Measurements of the spectrum and energy dependence of x-ray transition radiation*

Michael L. Cherry†
Enrico Fermi Institute and Department of Physics, University of Chicago, Chicago, Illinois 60637
(Received 2 August 1977)

We present the results of experiments designed to test the theory of x-ray transition radiation and to verify the predicted dependence of the characteristic features of the radiation on the radiator dimensions. We have measured the x-ray frequency spectrum produced by 5- to 9-GeV electrons over the range 4 to 30 keV with a calibrated single-crystal Bragg spectrometer, and at frequencies up to 100 keV with an NaI scintillator. The interference pattern in the spectrum and the hardening of the radiation with increasing foil thickness are clearly observed. We have also studied the energy dependence of the total transition-radiation intensity using a radiator with large dimensions designed to yield energy-dependent signals at very high particle energies, up to $E/mc^2 \approx 10^5$. The results are in good agreement with the theoretical predictions.

I. INTRODUCTION

A charged particle moving through a medium may radiate energy. The most common radiation processes are bremsstrahlung and Čerenkov radiation. A related phenomenon is transition radiation, which occurs when the incident particle crosses a sharp interface between two different media and rapidly rearranges its electromagnetic field, both in intensity and spatial extent. In the case of a highly relativistic ($\gamma = E/mc^2 \gg 1$) particle, most of the transition radiation is emitted at x-ray frequencies. The energy dependence of the radiation intensity is very different from that of bremsstrahlung or Čerenkov radiation. Typically, a strong increase of the transition radiation intensity is observed with increasing incident-particle Lorentz factor γ, up to extremely high values of γ. This feature makes x-ray transition radiation very useful for the detection of highly relativistic charged particles.

The intensity of the transition radiation emitted at a single interface is very weak. Therefore in practical applications[1-3] a radiator is used consisting of a large number N of thin foils, and radiation is produced at each of the $2N$ interfaces. The total intensity is then not just the sum of the intensities from the individual interfaces; rather, interference effects must be taken into account. In the case of a single interface, the intensity per unit frequency decreases monotonically with increasing frequency, and the total intensity is proportional to the Lorentz factor. However, with a radiation consisting of many foils, the interference effects lead to a frequency spectrum which exhibits strong oscillations, and to a saturation in the total intensity. The detailed calculations, summarized below, show that the positions of the interference maxima in the spectrum are governed largely by the radiator-foil thickness, and that the onset of saturation is determined by both the thickness and the spacing of the radiator foils.

The theoretical expressions for the intensity in the general case of many interfaces are quite complicated. However, the key features may be summarized in two relatively simple statements expressing the dependence of the radiation yield on the radiator parameters. We consider x-ray transition radiation of frequency ω generated by a relativistic particle of charge qe in a radiator of N foils of thickness l_1 separated by distances l_2 in a gas or vacuum. The plasma frequencies of the foil and gap materials are ω_1 and ω_2, respectively, where $\omega \gg \omega_1 \gg \omega_2$. In the usual case, the foil spacing is much larger than the thickness ($l_2 \gg l_1$), and the mass of the radiator is concentrated in the foils ($l_1\omega_1^2 \gg l_2\omega_2^2$). Then we expect the following:

(1) X-rays are emitted at frequencies below $\gamma\omega_1$, with a frequency spectrum which exhibits pronounced interference maxima and minima. At incident particle energies near or above saturation, most of the radiated intensity appears in the highest frequency maximum, at frequencies near $\omega_{\max} = l_1\omega_1^2/2\pi c$.

(2) The total emitted transition radiation increases with particle energy up to approximately

$$\gamma_S = E_S/mc^2 = 0.6\omega_1(l_1l_2)^{1/2}/c\,.$$

Saturation sets in above γ_S. Below γ_S, the total energy radiated is approximately proportional to γ:

$$S_N \approx \frac{2q^2\alpha\hbar}{3}\frac{(\omega_1-\omega_2)^2}{\omega_1+\omega_2}\gamma\frac{1-e^{-N(\sigma_1 l_1+\sigma_2 l_2)}}{\sigma_1 l_1+\sigma_2 l_2}\,, \qquad (1)$$

where $\alpha = e^2/\hbar c$, and σ_1^{-1} and σ_2^{-1} are the x-ray attenuation lengths evaluated at $\omega = \omega_{\max}$ in the foil and gap materials, respectively.

These simple rules are useful for qualitative estimates. More explicit predictions must be

made on the basis of the detailed theoretical calculations.[4-13] Various accelerator experiments[2,4,14-25] have been performed to test these calculations. The first and simplest tests were measurements of the average total intensity integrated over all frequencies and measured simultaneously with the ionization signal of the particle. The energy dependence and the saturation of the total intensity have been studied in such experiments[2,4,14-17] with electrons with $E \leq 15$ GeV ($\gamma \leq 3\times 10^4$) and radiators with $\gamma_S \lesssim 10^4$. For a more detailed test of the theory, measurements of the frequency spectrum have been attempted,[14,17-21] and in one such experiment,[20] the interference pattern and the hardening of the spectrum with increasing foil thickness have been observed. In none of these experiments, however, has the explicit dependence of ω_{max} or γ_s on l_1 and l_2 been investigated.

In this paper we present the results of a precise measurement of the frequency spectrum of the radiation produced by 5- to 9-GeV electrons. X rays were detected over the range 4 to 30 keV with an x-ray crystal spectrometer, and at frequencies up to 100 keV with an NaI scintillator. The details of the interference pattern and its dependence of the foil thickness l_1 were measured, and the experimental results are compared to the explicit theoretical calculations. As a further test of the theory, we have used the dependence of γ_S on l_1 and l_2 in order to design a radiator from which the radiation yield is energy dependent up to $\gamma_S \approx 10^5$, and have measured the total intensity produced in this radiator by electrons of 5 to 30 GeV. Before discussing the experimental results, we shall summarize the theoretical predictions and justify the two simple rules given above.

II. THEORETICAL PREDICTIONS

In reviewing the theoretical predictions, we follow closely the treatment in an earlier publication.[4] We briefly discuss the radiation emitted at a single interface, emphasizing the close relationship between transition radiation and Čerenkov radiation, and then proceed to the typical case of a radiator consisting of many thin foils. We first present the results in the absence of x-ray absorption, and then consider the more realistic case in which x-rays may be reabsorbed in the radiator. The treatment is based entirely on classical electrodynamics; quantum effects need to be considered only at high frequencies where pair production becomes possible.[5] We neglect the influence of multiple scattering of the incident particle on the emission of the radiation; this procedure is justified in Appendix A.

Consider the radiation emitted by a particle moving with uniform velocity $\vec{\beta}c$ along the trajectory $\vec{r}=\vec{\beta}ct$. The particle crosses the interface between two different media at time $t=0$ and at normal incidence, and emits radiation with intensity per unit solid angle and unit frequency derived from the Liénard-Wiechert potentials in the standard fashion[6]:

$$\frac{d^2S}{d\Omega d\omega} = \frac{1}{c}\left(\frac{qe\omega\beta\sin\theta}{2\pi}\right)^2 \times \left|\int_{-\infty}^{\infty} \epsilon^{1/4} e^{i\omega t(1-\epsilon^{1/2}\beta\cos\theta)} dt\right|^2, \tag{2a}$$

where we incorporate the dielectric "constant" ϵ into the time integral. The dielectric constant takes the form $\epsilon(t)=\epsilon_1$ for $t<0$ and $\epsilon(t)=\epsilon_2$ for $t>0$. In Eq. (2a), θ is the angle between the incident particle and the emitted photon. Immediately we see that the largest contribution to the integral comes from times[7]

$$\tau_{1,2} \lesssim \frac{1}{\omega(1-\epsilon_{1,2}^{1/2}\beta\cos\theta)},$$

and path lengths

$$\beta c\tau_{1,2} \lesssim \frac{\beta c}{\omega(1-\epsilon_{1,2}^{1/2}\beta\cos\theta)} = \frac{Z_{1,2}}{2}$$

in the two media. The lengths Z_1 and Z_2 (referred to as the "formation zones") characterize the distances from the interface in the respective media over which the transition radiation is generated. The integral can be evaluated over the pathlength from $-\beta cT$ to βcT, in the limit $T\to\infty$:

$$\int_{-\infty}^{\infty} \epsilon^{1/4} e^{i\omega t(1-\epsilon^{1/2}\beta\cos\theta)} dt = \lim_{T\to\infty} \frac{1}{i\omega}\left\{\epsilon_2^{1/4}\frac{e^{i\omega T(1-\epsilon_2^{1/2}\beta\cos\theta)}}{1-\epsilon_2^{1/2}\beta\cos\theta} - \epsilon_1^{1/4}\frac{e^{-i\omega T(1-\epsilon_1^{1/2}\beta\cos\theta)}}{1-\epsilon_1^{1/2}\beta\cos\theta} + \frac{\epsilon_1^{1/4}}{1-\epsilon_1^{1/2}\beta\cos\theta} - \frac{\epsilon_2^{1/4}}{1-\epsilon_2^{1/2}\beta\cos\theta}\right\}. \tag{2b}$$

The terms involving T are the Čerenkov terms, which vanish in the integration over angles except at the Čerenkov angles $\theta_{1,2}^C = \cos^{-1}(1/\epsilon_{1,2}^{1/2}\beta)$. The remaining terms describe the transition radiation, which vanishes when $\epsilon_1=\epsilon_2$. Squaring the integral over time and manipulating the Čerenkov terms,[6] we find that Eq. (2a) becomes

$$\frac{dS}{d\omega}=\frac{q^2e^2\omega}{c^2}\beta cT(\sin^2\theta_1^C+\sin^2\theta_2^C)+\frac{1}{c}\left(\frac{qe\omega}{4\pi c}\right)^2\int\sin^2\theta(\epsilon_1^{1/4}Z_1-\epsilon_2^{1/4}Z_2)^2d\Omega\,. \tag{3}$$

The first term gives the Čerenkov radiation generated between $-\beta cT$ and βcT, and the second term gives the transition radiation emitted at a single interface.[8-10]

In the limiting case of high energies and high frequencies (to which we restrict ourselves throughout this paper), the transition radiation is sharply peaked in the forward direction. If the dielectric constants are taken to be of the form $\epsilon_{1,2}=1-\omega_{1,2}^2/\omega^2$, then the most probable emission angle can be computed from the transition-radiation term in Eq. (3):

$$\theta_0\approx\left(\frac{1}{\gamma^2}+\frac{\omega_2^2}{\omega^2}\right)^{1/2}. \tag{4}$$

There may be considerable intensity, however, up to the angle

$$\theta_{\max}\approx\left(\frac{1}{\gamma^2}+\frac{\omega_1^2}{\omega^2}\right)^{1/2}. \tag{5}$$

Above $\theta_{\max}$, the transition-radiation intensity drops to zero because $\epsilon_1^{1/4}Z_1$ approaches $\epsilon_2^{1/4}Z_2$ in Eq. (3). The intensity decreases monotonically with increasing frequency, and drops away sharply at frequencies above $\gamma\omega_1$, since $\epsilon_1^{1/4}Z_1\approx\epsilon_2^{1/4}Z_2$ for $\omega\gg\gamma\omega_1$. In this limiting case of high energies, high frequencies, and small angles, the formation zones can be written as

$$Z_{1,2}=\frac{4c}{\omega}\left(\frac{1}{\gamma^2}+\frac{\omega_{1,2}^2}{\omega^2}+\theta^2\right)^{-1}, \tag{6}$$

and the transition-radiation intensity from a single interface is then given by

$$\frac{d^2S_0}{d\Omega d\omega}=\frac{1}{c}\left(\frac{qe\omega\theta}{4\pi c}\right)^2(Z_1-Z_2)^2. \tag{7}$$

The total transition-radiation intensity emitted at a single interface[9] is proportional to γ:

$$S_0=\frac{q^2\alpha\hbar}{3}\frac{(\omega_1-\omega_2)^2}{\omega_1+\omega_2}\gamma \tag{8}$$

This intensity is very weak—typically, the number of x rays emitted per interface is on the order of $\frac{1}{137}$. In order to enhance the x-ray signal to an observable level, one therefore uses radiators with a large number of interfaces. However, interference then leads to a saturation of the total intensity at high γ, and to a frequency spectrum characterized by oscillations about the single-interface spectrum. The characteristic features of the radiation are expressed in the two simple rules given in the Introduction, which express the dependence on the radiator dimensions. These are now justified, and the detailed results are given below.

A. Without absorption

In a radiator consisting of many thin foils separated by equal distances, the transition-radiation amplitudes for each interface must be added coherently.[4] In the absence of x-ray absorption, the radiation intensity per unit frequency is given by the familiar interference pattern[11,12]

$$\left.\frac{d^2S_N}{d\Omega d\omega}\right|_{\text{no abs}}=\frac{d^2S_0}{d\Omega d\omega}\,4\sin^2\frac{l_1}{Z_1}\frac{\sin^2N(l_1/Z_1+l_2/Z_2)}{\sin^2(l_1/Z_1+l_2/Z_2)}, \tag{9}$$

where $d^2S_0/d\Omega d\omega$ is the single-interface intensity from Eq. (7). The physical significance of this interference pattern can be understood as follows: In the rest frame of the rapidly moving particle, a resonance can exist between the wavelength λ' and the radiator period. In practice, the most important case is that of interference between the two interfaces of a single foil.[4,13] The amplitudes emitted at successive interfaces have opposite phase, as can be seen by interchanging the indices 1 and 2 in the integral of Eq. (2b). Therefore interference occurs when a half-integer multiple of λ' equals the period l_1'. Upon applying the Lorentz transformations to relate the frequency and foil thickness in the moving frame to those in the stationary laboratory frame, one obtains the resonance condition

$$l_1/Z_1=(2m+1)\pi/2\,,\quad m=0,1,2,3,\ldots\,. \tag{10a}$$

in the laboratory system. When interference is important both between the interfaces of a single foil and between those of a single gap, one finds the additional condition

$$l_1/Z_1+l_2/Z_2=m\pi\,,\quad m=1,2,3,\ldots\,. \tag{10b}$$

Equations (10a) and (10b) are just the conditions for the maxima in Eq. (9).

Equation (9) is strictly true only for normal incidence. However, it may be used in cases of nonnormal incidence[10] as long as the angle ψ between the incident trajectory and the interface is large compared to $\theta_{\max}$, and the dimensions l_1 and l_2 are measured along the trajectory—that is, one must make the substitutions $l_{1,2}\to l_{1,2}/\sin\psi$.

In most experiments, the observed quantity is the intensity integrated over all angles. The integration of Eq. (9) has been performed analytically by Ter-Mikaelian[7,11] and Garibian[10,12]:

$$\left.\frac{dS_N}{d\omega}\right|_{\text{no abs}} = 2Nq^2e^2(l_1+l_2)^2\frac{(\omega_1^2-\omega_2^2)^2}{\omega^2}$$

$$\times\sum_{r=r_{\min}}^{r_{\max}}\left\{\sin^2\left[\frac{l_2}{l_1+l_2}\left(\frac{l_1}{4\omega c}(\omega_1^2-\omega_2^2)-\pi r\right)\right]\right.$$

$$\left.\times\frac{2\pi cr-(l_1+l_2)\omega/2\gamma^2-(l_1\omega_1^2+l_2\omega_2^2)/2\omega}{[l_1(\omega_1^2-\omega_2^2)/2\omega-2\pi cr]^2[l_2(\omega_2^2-\omega_1^2)/2\omega-2\pi cr]^2}\right\}. \tag{11a}$$

The summation is performed over integers r in the range $r_{\min}\leq r\leq r_{\max}$, where

$$r_{\min}=\frac{l_1+l_2}{2\pi\gamma c}\left(\frac{l_1\omega_1^2+l_2\omega_2^2}{l_1+l_2}\right)^{1/2} \quad \text{and} \quad r_{\max}=\gamma r_{\min}. \tag{11b}$$

Equation (11a) is valid over the frequency range

$$\gamma^2\left\{\frac{2\pi cr}{l_1+l_2}+\left[\left(\frac{2\pi cr}{l_1+l_2}\right)^2-\frac{l_1\omega_1^2+l_2\omega_2^2}{\gamma^2(l_1+l_2)}\right]^{1/2}\right\}\geq\omega\geq\gamma^2\left\{\frac{2\pi cr}{l_1+l_2}-\left[\left(\frac{2\pi cr}{l_1+l_2}\right)^2-\frac{l_1\omega_1^2+l_2\omega_2^2}{\gamma^2(l_1+l_2)}\right]^{1/2}\right\}. \tag{11c}$$

The bulk of the intensity is due to the terms near $r=r_{\min}$.

An example of the frequency spectrum (11) is plotted in Fig. 1. Also shown is the corresponding single-interface spectrum $dS_0/d\omega$ obtained by integrating Eq. (7) over angles. The characteristic oscillations of the many-foil spectrum about the single-interface spectrum are evident. Maxima in the spectrum appear at the extrema of the sine function in Eq. (11a), at frequencies determined by the radiator dimensions and the plasma frequencies. At sufficiently high energies, where $r_{\min}\leq 1$, most of the radiation is emitted near the last maximum in the spectrum. In the usual limit $l_2\gg l_1$, this maximum appears near a characteristic frequency determined by the thickness of the radiator foils[4]:

$$\omega_{\max}=\frac{l_1\omega_1^2}{2\pi c}. \tag{12}$$

The total energy radiated can be computed by numerically integrating Eq. (11a) over frequency. The result of such an integration is shown in Fig. 2. The smooth curves give the total many-foil intensities, normalized by the number of interfaces, for three different radiators. The dashed line is the single-interface intensity from a CH_2/He interface, $S_0=0.05\gamma$ eV [Eq. (8)]. The many-foil

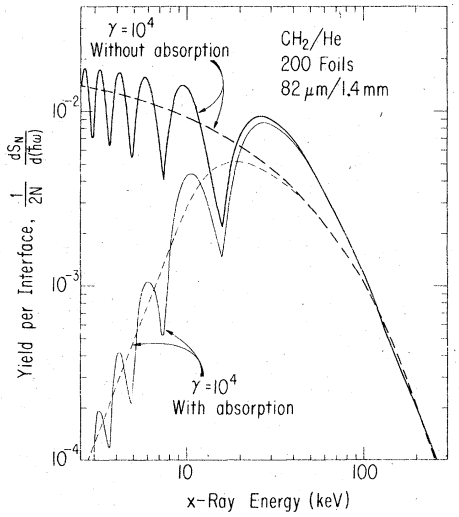

FIG. 1. Comparison of x-ray energy radiated per keV per interface by a singly-charged particle, $(1/2N)dS_N/d(\hbar\omega)$ for a many-foil radiator (solid lines), and $dS_0/d(\hbar\omega)$ for a single CH_2/He interface (dashed lines). Curves are shown with absorption in the radiator (light lines) and without absorption (heavy lines). The many-foil radiator is CH_2/He with $N=200$, $l_1=82$ μm, and $l_2=1.4$ mm.

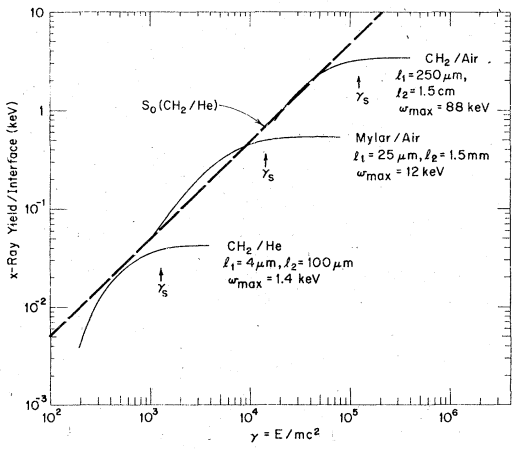

FIG. 2. Total energy radiated per interface in the absence of absorption for a single CH_2/He interface (dashed line) and for three different many-foil radiators (solid lines), as a function of Lorentz factor. Arrows mark the saturation energies γ_S predicted from Eq. (14c).

curves follow the single-interface prediction approximately at low energies. As the energy increases, additional terms with low r enter the sum in Eq. (11a) until the energy is so high that $r_{\min} \leq 1$ and there are no remaining terms to contribute. The intensity then saturates. The largest contribution to the intensity comes from the $r=1$ term. We define the Lorentz factor $\gamma_S(\omega)$ marking the onset of saturation at a particular frequency ω such that this first term approaches its limiting value at infinitely large γ:

$$\frac{dS_N/d\omega(r=1,\gamma=\gamma_S(\omega))}{dS_N/d\omega(r=1,\gamma\to\infty)} = 1-\delta, \quad \text{where } \delta \ll 1. \tag{13}$$

Then, using the explicit expression (11a), we can derive

$$\gamma_S(\omega) = \alpha\left(\frac{l_2\omega}{c}\right)^{1/2}, \tag{14a}$$

where

$$\alpha^2 = \frac{1}{4\pi\delta}\,\frac{1+l_1/l_2}{1-\omega_{\max}/2\omega - l_2\omega_2{}^2/2\omega}. \tag{14b}$$

[From (11c) and the condition $r_{\min} \leq 1$, it can be verified that α^2 is always positive.] At high energies, the bulk of the intensity is generated near $\omega_{\max}$, so saturation in the total yield occurs near $\gamma_S(\omega_{\max})$. If we choose $\delta = 0.07$, then (in the limit $l_1\omega_1{}^2 \gg l_2\omega_2{}^2$ and $l_2 \gg l_1$)

$$\gamma_S = \gamma_S(\omega_{\max}) = 0.6\omega_1(l_1l_2)^{1/2}/c. \tag{14c}$$

Figure 2 demonstrates that this expression for γ_S is quite accurate over a wide range of Lorentz factors and radiator dimensions.[26]

B. With absorption

The effect of x-ray absorption in the radiator may be evaluated by assuming that the x rays are initially emitted at random depths in the radiator. Then the average fraction $\eta(\omega)$ of emitted x rays which actually escape from the end of the radiator is

$$\eta(\omega) = \frac{1-e^{-N(\sigma_1l_1+\sigma_2l_2)}}{N(\sigma_1l_1+\sigma_2l_2)}, \tag{15}$$

where $\sigma_{1,2}{}^{-1}(\omega)$ are now the x-ray attenuation lengths at the frequency ω. We assume the absorption in a single foil is small. η is a monotonically varying function of ω (except near absorption edges) which approaches unity for weak absorption (high frequencies) and decreases to $1/N(\sigma_1l_1+\sigma_2l_2)$ for strong absorption (low frequencies). The intensity per unit frequency can then be written,[10]

$$\frac{dS_N}{d\omega} = \eta(\omega)\left.\frac{dS_N}{d\omega}\right|_{\text{no abs}}. \tag{16}$$

A different approach is to perform the coherent summation of the radiation amplitudes from each interface with complex dielectric constants,[13] leading to the following form of the interference pattern[10]:

$$\frac{d^2S_N'}{d\Omega d\omega} = \frac{d^2S_0}{d\Omega d\omega}\,e^{-(N-1)(\sigma_1l_1+\sigma_2l_2)/2}\,4\sin^2\frac{l_1}{Z_1}\,\frac{\sinh^2[(N/4)(\sigma_1l_1+\sigma_2l_2)]+\sin^2N(l_1/Z_1+l_2/Z_2)}{\sinh^2[\frac{1}{4}(\sigma_1l_1+\sigma_2l_2)]+\sin^2(l_1/Z_1+l_2/Z_2)}. \tag{17}$$

For the radiators used in our experiments, we have verified that the numerical integration of Eq. (17) over angles leads to a frequency spectrum identical to that of Eq. (16). An example of this spectrum is plotted in Fig. 1. Its structure closely resembles that of the spectrum without absorption except that the radiation intensity is suppressed at low frequencies.

As long as the effect of absorption is small near $\omega_{\max}$, the qualitative features discussed earlier remain essentially unchanged. For example, in Fig. 3 are shown four frequency spectra, including absorption, with $N=200$, $l_2=1.4$ mm, and l_1 ranging from 16 to 82 μm. Arrows mark the positions of $\omega_{\max}$. For the thin foils, the suppression of the low-frequency intensity by absorption leads to calculated curves with maxima somewhat higher than $\omega_{\max}$. For the thicker foils, displacements are due to inaccuracies introduced by the assumption $l_2 \gg l_1$ in the derivation of Eq. (12); when the condition $l_2 \gg l_1$ is not well satisfied, the positions of the maxima are shifted slightly to lower frequencies.[4]

At energies below saturation, the radiation emitted per interface, integrated over all frequencies, is approximately $S \approx \eta(\omega_{\max})S_0$, where S_0 is the total single-interface intensity given in Eq. (8). The total energy radiated is then

$$S_N \approx 2N\eta(\omega_{\max})S_0 \tag{18}$$

below saturation, in agreement with Eq. (1).

We have tested these predictions experimentally. Our results are described in the following sections.

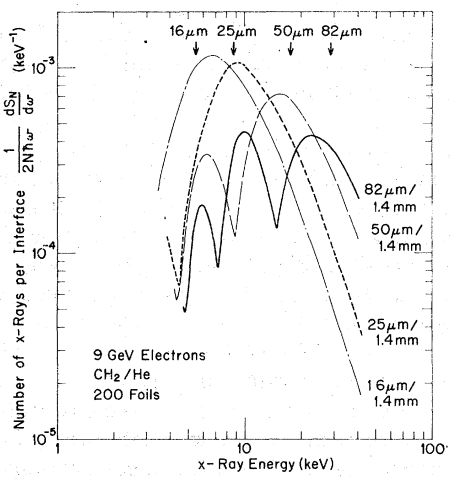

FIG. 3. Number of x rays emitted per keV per interface, $(1/2N\hbar\omega)dS_N/d(\hbar\omega)$ (keV^{-1}), with absorption. Spectra are plotted for four values of foil thickness l_1 (16, 25, 50, and 82 μm). Arrows mark the frequencies ω_{max} given by Eq. (12) for each value of l_1.

III. MEASUREMENTS OF THE FREQUENCY SPECTRUM

A measurement of the transition-radiation frequency spectrum requires: (1) that the incident particle be deflected from the detector in order to avoid contributions to the measured signal due to the ionization loss of the particle in the detector; (2) that the detector be capable of resolving the structure in the interference pattern; and (3) that the detector be capable of distinguishing between single-photon events and events due to two or more photons. In previous experiments.[14,17-21] the incident particles were magnetically deflected and a scintillator, solid-state detector, or proportional counter was placed directly in the x-ray beam and pulse-height analyzed. However, it is not possible with this technique to fulfill condition (3)—that is, one cannot differentiate between a single x-ray and several simultaneous x-rays with the same total energy. One therefore measures only the total intensity emitted per incident particle rather than the single-photon spectrum given by Eq. (16). This difficulty can be circumvented by using very short radiators to minimize the probability of emission of more than one x ray. Fabjan and Struczinski[20] have observed the resulting interference pattern in this fashion with $N<30$. In the present experiment, all three conditions are fulfilled. Using a high-resolution Bragg crystal spectrometer, we have directly observed the single-photon spectrum without resorting to untypically short radiators.

The radiators used with the crystal spectrometer are listed in the first part of Table I. They consist of evenly spaced polypropylene (CH_2) foils or of polyethylene (CH_2) foam, with dimensions and total lengths typical of the applications in which transition radiation detectors have thus far been used[1-3] (i.e., they are characterized by $\gamma_S \approx 10^4$ and $\omega_{max} = 6-30$ keV). We have used the spectrometer to measure the single-photon spectrum produced in these radiators over the frequency range 4 to 30 keV. The measurements and the results are presented in Sec. A below.

The radiators in the second part of Table I have large dimensions appropriate for higher energies ($\gamma_S \approx 10^5$) and higher frequencies ($\omega_{max} = 86$ keV). In order to study the spectrum from these radiators at frequencies up to 100 keV, we have performed measurements with an NaI scintillator in the direct x-ray beam. In this case, multiphoton events had to be taken into account. The results are discussed in Sec. B.

This large variation in radiator dimensions was chosen in order to study the theoretical predictions over a wide range of frequencies.

A. Crystal measurements

The experiment was performed at the Cornell Synchrotron. Figure 4 shows the experimental

TABLE I. Radiator parameters.

Materials	l_1 (cm)	l_2 (cm)	ω_1 (eV)	ω_2 (eV)	N	l_2/l_1	ω_{max} (keV)	γ_S	$\gamma_S\omega_1$ (keV)	ω_{MS} (MeV) ($\chi=0.6$)
CH_2/He	1.6×10^{-3}	0.14	21	0.3	1000	88	5.6	9.5×10^3	199	5.1
CH_2/He	5.0×10^{-3}	0.14	21	0.3	250	28	18	1.7×10^4	351	1.7
CH_2/He	8.2×10^{-3}	0.14	21	0.3	200	17	29	2.2×10^4	450	1.1
Ethafoam (CH_2/Air)	3.0×10^{-3}	0.10	21	0.7	300	33	11	1.1×10^4	230	2.1
CH_2/Air	2.44×10^{-2}	0.75	21	0.7	200	31	86	8.6×10^4	1800	1.9
CH_2/Air	2.44×10^{-2}	1.5	21	0.7	100	61	86	1.3×10^5	2500	3.8

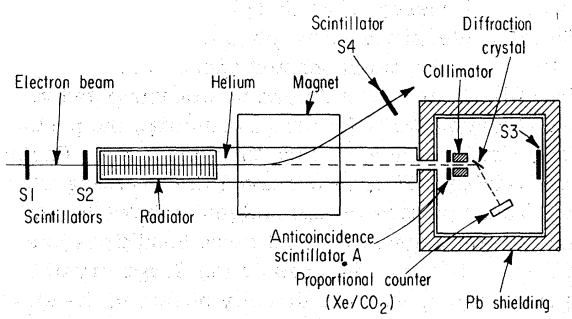

FIG. 4. Experimental setup for the crystal measurements.

arrangement. Electrons of 5 and 9 GeV produced transition radiation in the radiator, and were deflected away from the x-ray detector with a magnet. The x rays passed through a 6-m-long helium path and a 0.5 cm wide collimator. This narrow collimator aperture ensured that the entire crystal face was illuminated at small Bragg angles. The scintillators S1, S2, S3, and A (where A had an opening through the center matching the dimensions of the collimator aperture) were used to determine the intensity and spatial distribution of the incident electron beam. Since the x-ray intensity per electron was quite low, we required very high incident electron intensities and therefore did not trigger on individual electrons. The total electron intensity for each run was determined by monitoring the number of coincidences $S1 \cdot S2$. With the magnet current off, we measured the fraction $\varphi = S1 \cdot S2 \cdot S3 \cdot \bar{A}/S1 \cdot S2$ of electrons whose trajectories passed through the collimator. This fraction varied from $\varphi \approx 20\%$ at 5 GeV to $\varphi \approx 50\%$ at 9 GeV. In order to normalize the measured x-ray intensity to the electron flux, to first order we considered the measured x-ray intensity to be due to a flux of parent electrons of intensity $\varphi S1 \cdot S2$. This approximation depends on the assumption that the transition-radiation x rays follow the trajectory of their parent electrons in the absence of a magnetic field. In the comparison below of the measured data and the theoretical predictions, we take into account the detailed angular distribution of the x rays [Eq. (9)]. This calculation requires a knowledge of the shape and angular distribution of the incident electron beam, which depends on the accelerator beam focusing and on the effects of the multiple scattering of the electrons. We have derived the electron angular distribution from measurements of the diameter of the electron beam incident on scintillator S1, measurements (with the magnet off) of the fraction ϕ of electrons passing through the collimator with various thicknesses of plastic (0–2.5 cm) in the beam, and measurements of the variation of φ as the beam was steered across the collimator aperture. These tests were performed frequently throughout the runs in order to check the value of φ and to monitor changes in the focusing, alignment, and distribution of the electrons.

The spectrometer consisted of a lithium fluoride (LiF) or a pentaerythritol (PET) crystal and a xenon/CO_2 proportional counter (5 cm thick, 1.5 atmospheres) whose output was pulse-height analyzed. The xenon counter was calibrated and checked periodically during the runs with x-ray sources—^{55}Fe (5.9 keV), ^{113}Sn (25 keV), and ^{137}Cs (32 keV). The crystals were sensitive to x-rays over the range 4–30 keV, and were calibrated over that frequency range with laboratory x-ray machines. The results of these calibrations are shown in Fig. 5, where the quantity plotted is the effective width $\delta\epsilon$ for each crystal. The effective width is a measure of the range of x-ray energies at a given Bragg angle over which x rays are diffracted. Since we are interested in measuring effects which vary over x-ray energy ranges large compared to the crystal resolution, we treat the crystal as if its scattering efficiency at a given angle were 100% over an energy range of width $\delta\epsilon$ about the Bragg energy, and zero at all other energies (i.e., we approximate the response of the crystal by a square function). The points shown in Fig. 5 are measured effective widths; the smooth curves are the theoretically expected maximum and minimum effective widths for extreme crystal-surface conditions. The characteristics of the crystals and the details of the calibrations are discussed in Appendix B. The excellent resolution provided by the crystals, and the requirement that the Bragg condition be fulfilled, account for the elimination of multiphoton events. Photo-

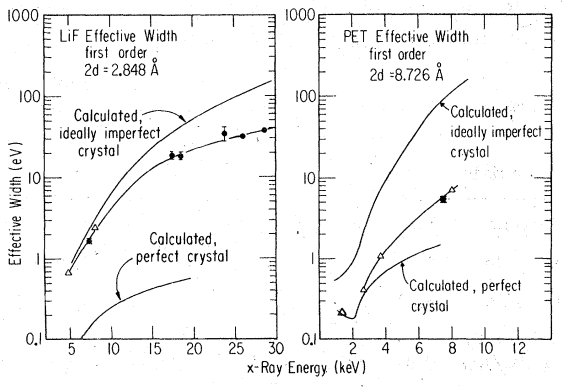

FIG. 5. Effective widths of LiF and PET crystals. Solid points are measured with balanced filters; open triangles are measured with fluorescence lines. Calculated curves are theoretical limiting cases of maximum and minimum effective widths.

electric absorption was computed on the basis of tabulated x-ray cross sections,[27,28] giving the probability of an x ray at the Bragg energy propagating from the radiator to the xenon counter and then being absorbed in the detector. This probability increased from 53% at 4 keV to 96% at 10 keV due to the increasing transparency of the intervening material, and then decreased to 27% at 30 keV due to the decreasing detector efficiency. The combination of the high crystal resolution and the inherent weakness of the radiation process led to fairly low counting rates and required that special efforts be devoted to shielding the apparatus and minimizing background.

Figure 6 shows two superimposed pulse-height distributions measured with the LiF crystal set for 9.1 keV x rays. One distribution was generated with a radiator in the beam; in the other distribution the radiator was replaced by a solid block of polyethylene of the same total mass. This background test has been performed for every run. The transition radiation peak at 9 keV is well resolved from background, and at 18 keV a small second-order scattering peak can be seen. The fraction of 9-keV x rays which arrive simultaneously and masquerade as single 18-keV x rays is less than 10^{-3}. The width of the x-ray peaks in Fig. 6 is determined by the resolution of the proportional counter and not by the resolution of the crystal. The vertical scale is x rays per 10^5 electrons in S1·S2. Because of the high resolution of the crystal and the low x-ray intensity, more than 10^3 electrons were needed for each 9-keV x-ray count.

In Fig. 7 are shown the results of our measurements for three radiators with different foil thicknesses, plotted as the number of x rays per interface normalized to the measured number of parent

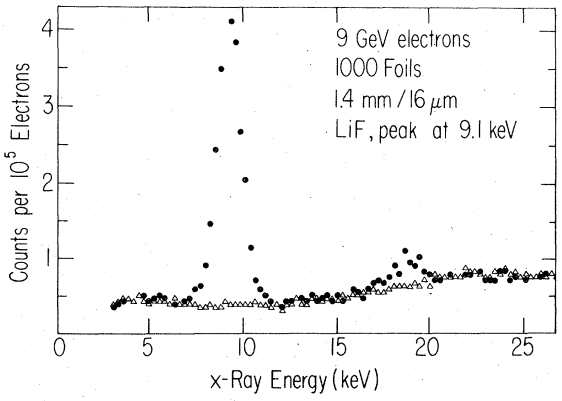

FIG. 6. Pulse-height distributions measured in the proportional counter. The solid points show transition radiation from 1000 CH_2 foils, and the open triangles are obtained with a background radiator.

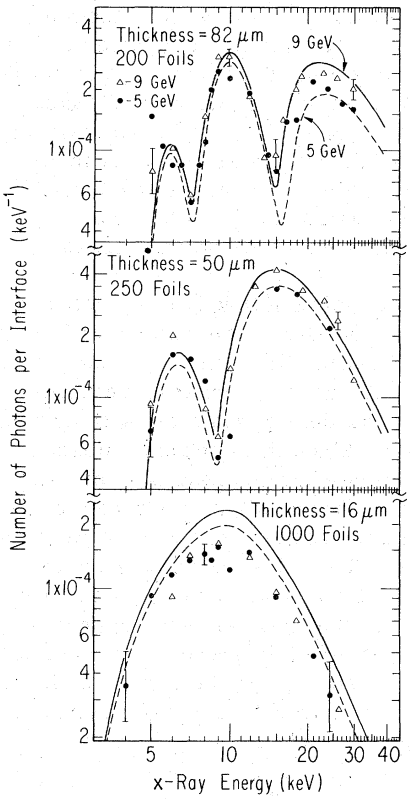

FIG. 7. Number of transition-radiation x rays per keV per interface emerging from three CH_2/He radiators with different foil thicknesses. The points (solid points for 5-GeV and open symbols for 9-GeV electrons) are measured data; and the curves (dashed lines for 5 GeV and solid lines for 9 GeV) are calculated spectra.

electrons φS1·S2. The foils are polypropylene spaced by 1.4 mm of helium, with thicknesses 16–82 μm. The number of foils in each radiator (200–1000) is chosen such that the total mass (and hence the photoelectric absorption and multiple scattering) is approximately the same in each case. The data points are corrected for the efficiency of the crystal and the xenon counter, and for the transmission of the absorbing material (mainly helium) between the radiator and spectrometer. Typical error bars are shown. They are due to the uncertainty in the crystal calibrations, small changes in the electron-beam focusing, and, at low intensities, uncertainties in the background subtraction.

The curves in Fig. 7 are theoretically predicted spectra. These are derived from Monte Carlo calculations based on the interference pattern of Eq. (9), which gives the frequency and angular distribution of the radiation. The calculations take into account the angular distribution of the incident electrons and the absorption in the radiator

calculated for each x-ray as a function of its individual starting point in the radiator. Uncertainties in the x-ray cross sections and the statistics of the Monte Carlo calculations introduce an uncertainty of up to ±5% into the calculations. Our measured intensities are systematically lower than the predicted intensities by about 15%. The calculated values in Fig. 7 are therefore multiplied by a constant overall normalization factor of 0.85.

The data points follow the calculated spectral shapes excellently. The maxima and minima due to interference effects are well resolved and appear exactly at the calculated frequencies. The radiation hardens as expected with increasing foil thickness. Since these measurements are made with particle energies near or above saturation, the bulk of the radiation is expected close to the last maximum in the spectrum, near $\omega_{max} = l_1\omega_1^2/2\pi c$ [Eq. (12)]. This expression assumes the radiator to be transparent at ω_{max}, and it further assumes that the spectral shape is primarily determined by single foil interference (i.e., $l_2 \gg l_1$). For the 82 and 50 μm radiators, the last maxima are measured at 23 and 15 keV, respectively, while $\omega_{max} = 29$ and 18 keV. As discussed in Sec. II, this small shift in frequency arises because the condition $l_2 \gg l_1$ is not well satisfied. In the case of the 16 μm radiator, with a measured maximum at 9 keV ($\omega_{max} = 6$ keV), reabsorption at low frequencies strongly influences the spectral shape and suppresses the low-frequency structure.

Saturation is expected at electron energies between 5 and 11 GeV. Consequently very little energy dependence is noticeable in the measured spectra. The saturation energy should increase slightly with increasing foil thickness, and in fact a small energy dependence appears to be present in the results for the thicker radiators near ω_{max}.

We have presented preliminary results in an earlier publication[29] in which the measured data points were compared to the spectrum (16) computed without taking into account effects due to the angular distributions. The calculated spectral shape matched the measured spectrum very well, but the measured values fell below the calculated curves by about 36%. In the present calculations this discrepancy has been reduced to 15% by taking into account the effects of the angular distributions of both the x-rays [Eq. (9)] and the electrons. However, the calculations of the electron distribution neglect halos around the beam, scattering from beam pipes, and other detailed irregularities in the beam which tend to broaden the angular pattern. Such effects, coupled with the various experimental and computational uncertainties mentioned above, are undoubtedly the major cause of the remaining 15 % discrepancy in the absolute scale. This discrepancy does not indicate a significant departure from the theoretically expected behavior.

We have also measured the frequency spectrum of a plastic foam radiator (Ethafoam, manufactured by Dow Chemical Co.). Ethafoam is a closed-cell polyethylene foam composed of irregularly shaped cells of diameter approximately 1 mm and wall thickness about 30 μm. The gas inside the cells is air. Previous accelerator tests[25] have shown that the total yield from an inhomogeneous foam radiator with average wall thickness $\langle l_1 \rangle$ and cell diameter $\langle l_2 \rangle$ is approximately the same as that from a foil radiator composed of the same materials and with equal l_1, l_2, and total length. This is expected if the deviations of the cell dimensions from the average are sufficiently small.[30] The light weight, convenience, and relative inexpensiveness of foam radiators compared to foil radiators make them attractive for large scale practical applications. In particular, Ethafoam has been used as the radiator material in the balloon-borne transition-radiation detector for high-energy cosmic-ray electrons described in Ref. 1.

The spectrum of the radiation emitted by 5 GeV electrons in a 30 cm long Ethafoam radiator, measured with the LiF crystal, is shown in Fig. 8. The smooth curve is the theoretical spectrum, calculated and normalized as above, for an equivalent foil radiator with $N = 300$ and dimensions $l_1 = 30$ μm and $l_2 = 1$ mm. Reabsorption due to the air inside the cells suppresses the low-frequency points, but the spectrum peaks near ω_{max} as expected. The measured peak appears between 10

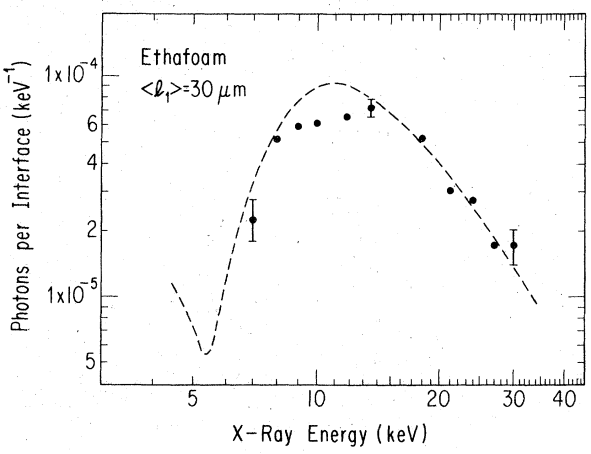

FIG. 8. Frequency spectrum produced by 5-GeV electrons in Ethafoam. The solid points are measured results. The curve is calculated for an equivalent CH_2/air foil radiator with $N = 300$, $l_1 = 30$ μm, and $l_2 = 1$ mm.

and 15 keV, and fits well with the sequence shown in Fig. 7 of peak positions increasing with increasing foil thickness. The good agreement between the measurements and the calculated curve provides further confirmation of the similar behavior of foil and foam radiators.

B. Direct-beam measurements

The crystal spectrometer was used up to 30 keV. In order to measure the total radiation intensity per incident electron generated in radiators with large dimensions at frequencies up to 100 keV, we replaced the spectrometer with a thin NaI scintillator directly in the x-ray beam. The scintillator was 0.37 mm thick, and had an x-ray detection efficiency of 26% at 86 keV and 10% at 130 keV. The absolute x-ray energy scale was obtained by calibrating with ^{55}Fe (5.9 keV), ^{113}Sn (25 keV), ^{241}Am (60 keV), ^{133}Ba (31, 80 keV), and ^{57}Co (6, 14, 122 keV) x-ray sources. The radiators consisted of polypropylene foils in air, with $N = 200$, $l_1 = 244$ μm, $l_2 = 0.75$ cm, and $N = 100$, $l_1 = 244$ μm, $l_2 = 1.5$ cm. Runs were made at an electron energy of 6.4 GeV.

The direct-beam observations required much lower beam intensities than did the crystal measurements. We were therefore able to trigger on individual electrons. For each event, a coincidence $S1 \cdot S2 \cdot b$ was required, where b was an external beam pulse which marked the accelerator beam spill. The trigger effectively removed contributions from the general room background. However, since we now derived the spectral shape entirely from the pulse height analysis, contributions due to neutral background coming down the beam line in association with the electrons could not be separated from the transition radiation. We performed runs to measure the intensity and spectrum of the background by replacing the radiators with solid blocks of plastic in the beam with thicknesses equal to the total radiator thicknesses.

In Fig. 9 are shown pulse-height distributions obtained with the two radiators. The smooth curves are the result of Monte Carlo calculations. These calculations are based on the single-photon distribution (9) and use the same angular distribution and overall normalization as described above. Each x ray emitted by a given electron is individually propagated through the radiator, the absorber material, the collimator, and the detector. Escape of fluorescence photons and photoelectrons, and fluctuations arising from the detector resolution, are taken into account. This gives the distribution of the total x-ray signal per incident electron, which must then be folded together with

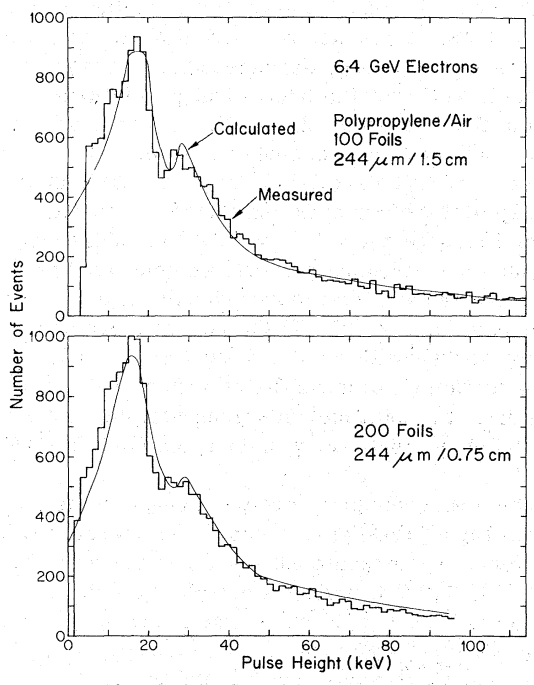

FIG. 9. Pulse-height distributions measured with the NaI scintillator directly in the x-ray beam. Smooth curves are calculated distributions.

the measured background distribution. The curves in Fig. 9 are the result of this convolution. The measured and calculated distributions agree very well.

It must be realized that these direct-beam measurements show intrinsically less sharp structure than the distributions measured with the spectrometer. This is due to the presence of background and multiple-x-ray events, and to the poorer detector resolution. However, the expected structure can still be seen. Although the last maximum, near 86 keV, does not appear because the electron energy is a factor of 7–10 below saturation (see Table I), the next two maxima are observed at 28 and 17 keV as expected. The spectra measured in the two radiators (which differ only in the number of foils N and the foil spacing l_2) are nearly identical, confirming that the spectrum depends on the foil thickness l_1, and not on l_2 or N (provided that $l_2 \gg l_1$).

IV. HIGH-ENERGY MEASUREMENTS OF THE TOTAL INTENSITY

Experiments which have measured the energy dependence of transition radiation[2,4,14-17] have generally been performed with electrons with $E \leq 15$ GeV ($\gamma \leq 3 \times 10^4$). In those experiments[22-24,31,32] in which transition-radiation signals have been observed at electron energies above 15 GeV, the

radiation has been in saturation. In all these experiments, performed with radiators with $\gamma_S \lesssim 10^4$, the measured energy dependence has agreed reasonably well with the theoretical predictions. From the discussion of Sec. II, however, one sees that with the proper choice of parameters it is possible to design a radiator with γ_S as large as 10^5. We have therefore built and tested a transition radiation detector with $\gamma_S = 1.3 \times 10^5$. Measurements of the frequency spectrum generated by 6.4-GeV electrons in two radiators with high γ_S were presented in Sec. III. These results were shown to agree well with the theoretical predictions. In this section we discuss the results of measurements of the total intensity generated in such a radiator by electrons with energies from 5 to 30 GeV.

The measurements were performed on the M5 beam line of the Fermi National Accelerator Laboratory. The experimental setup is shown in Fig. 10. T1, T2, T3, and T4 were plastic scintillators used to define the beam. A was a plastic anticoincidence scintillator with a hole through its center. The Čerenkov counter Č and the shower counter S (consisting of lead and plastic scintillator T5) were used to select electrons and reject protons, pions, and kaons. The fraction of electrons in the beam decreased from 40% at 5 GeV to 1% at 30 GeV. The radiator consisted of 200 polypropylene foils with thickness 2.44×10^{-2} cm and spacing 1.5 cm. The x-ray detector was the same 0.37-mm-thick NaI scintillator described in Sec. III.

An event was accepted if a coincidence $\check{C} \cdot T1 \cdot T2 \cdot T3 \cdot T4 \cdot \bar{A} \cdot S$ was observed. For each event, the outputs from Č, T2, T3, T4, S, and the NaI detector were then simultaneously and independently pulse-height analyzed and recorded on tape. Lower limits were set for the Čerenkov counter and shower counter pulse heights to ensure that only electrons were accepted. The beam intensity was kept sufficiently low so that there were very few multiparticle events, which could then be eliminated in the data analysis by applying strict upper limits to the T2, T3, and T4 scintillator signals.

Measurements were made at 5, 15, and 30 GeV

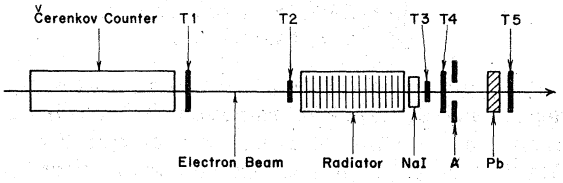

FIG. 10. Experimental setup for measurements of the total intensity.

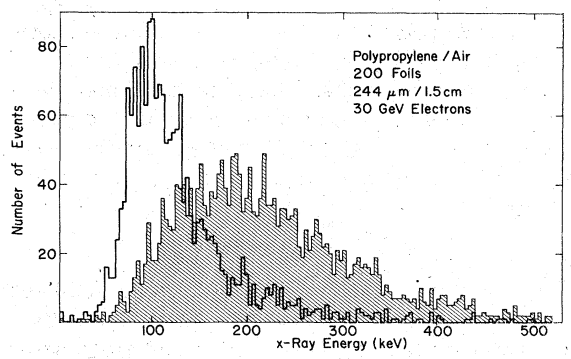

FIG. 11. Pulse-height distributions measured in the NaI scintillator. These distributions were measured without magnetic deflection. The Landau-type distribution (heavy line) was observed with a solid polyethylene background block in the beam. The shaded distribution was obtained with a radiator with thick foils and large spacings ($N = 200$, $l_1 = 244$ μm, $l_2 = 1.5$ cm, $\omega_{max} = 86$ keV, $\gamma_S = 1.3 \times 10^5$). The distributions are normalized to the same number of events.

both with the radiator in the beam and with a solid 2 in. block of polyethylene in its place. Two pulse-height distributions obtained at 30 GeV are shown in Fig. 11. The unshaded histogram is measured with the background block in place. It shows the expected Landau-type shape due primarily to ionization losses in the detector, with an average pulse height of 132 ± 1 keV. With the plastic foils in the beam, the distribution is shifted to higher energies due to the presence of transition radiation. The average pulse height is now 226 ± 3 keV. Note that the structure of the frequency spectrum shown in Fig. 9 is completely washed out by the presence of the ionization background.

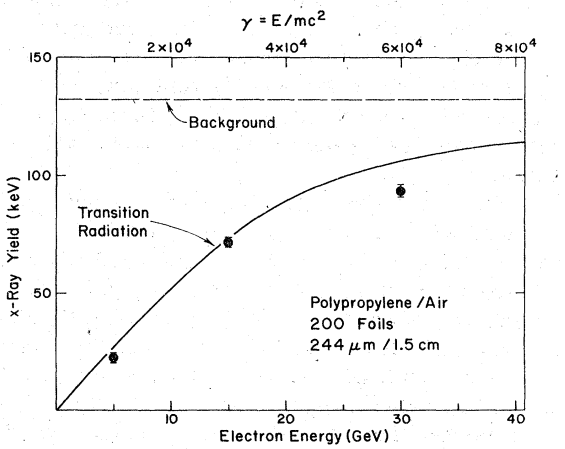

FIG. 12. Energy dependence of total transition-radiation intensity. The points are measured values, the smooth curve is the calculated transition radiation yield, and the dashed line is the average measured background signal in the scintillator.

The average measured transition-radiation energy (i.e., the difference between the average pulse heights with and without the radiator) is plotted in Fig. 12 as a function of electron energy. Also plotted are the theoretical predictions obtained from a Monte Carlo calculation similar to that used for the direct-beam analysis. In this case, however, we include the ionization loss of the electrons in the scintillator and neglect the effects of the angular distribution. There is no correction for the overall normalization. The measured data points agree quite well with the calculated results.

The two distributions shown in Fig. 11 are well separated. With some additional experimental sophistication (such as the application of pulse-shape-discrimination techniques, or the use of a thinner detector or multiple radiators and detectors to provide even better separation), such radiators can be applied to the measurement of particle energies as high as $\gamma_S = 10^5$. However, a major limitation at high energies is the total length of the radiator, which may become prohibitive for large solid angle and large area experiments.

V. CONCLUSIONS

There are two aspects of this work to be considered. First, our understanding of the basic physical mechanism of x-ray transition radiation is quite accurate. The detailed theoretical predictions, based on classical electrodynamics without corrections to the radiation intensity due to multiple scattering, are in good agreement with our measurements of the frequency spectrum and of the total intensity. The significance of the radiator dimensions l_1 and l_2, which is essential to optimum experimental applications, is well understood. The foil thickness l_1 governs the frequency ω_{max} at which the final maximum in the interference pattern appears, and the product of l_1 times the spacing l_2 determines the saturation energy γ_S. This is confirmed by the observations of the structure of the interference pattern and the hardening of the spectrum with increasing l_1, and further indicated by the results on the energy dependence at $\gamma \geq 10^4$ obtained by using large radiator dimensions.

Second, we may consider the experimental significance of the agreement between the measured results and the calculations. The importance of the spectral measurements, and of the demonstration of the dependence of the spectrum on l_1, is connected with the possibility of "tuning" the radiator dimensions and detector thickness. In practical applications, it is very important to choose the foil thickness such that the frequency range near ω_{max} coincides with the sensitive region of the detector. Another aspect of all experimental applications is the energy dependence. The effect of the dimensions on the energy dependence has been illustrated in Fig. 2. This figure shows clearly that with the proper choice of the radiator parameters l_1 and l_2, it is possible to use transition-radiation detectors over a wide range of incident-particle Lorentz factors. So far, only radiators with $\gamma_S \approx 10^4$ have been used for the purpose of particle identification. As shown in Fig. 2, it is feasible to obtain energy-dependent signals over the wide range $300 \lesssim \gamma \lesssim 10^5$, and to use transition-radiation detectors to measure particle energies over that range. The technique is limited at high γ because radiator dimensions become very large for $\gamma_S \gtrsim 10^5$. For low γ, the low intensities and the experimental difficulties involved in using soft x rays appear to restrict x-ray transition-radiation detectors to $\gamma_S \gtrsim 300$. Within these limits, however, such detectors can be used for a variety of applications, including observations of hadrons at accelerators[16] and measurements of the fluxes of high-energy cosmic-ray muons and nuclei.[31,32]

ACKNOWLEDGMENTS

The author is extremely grateful for the support and the assistance of his faculty advisor, Professor Dietrich Müller. Doctor R. L. Blake of Los Alamos offered invaluable advice and loaned us the essential parts of the spectrometer. We appreciate the help of D. Barrus during the fluorescence line calibrations, and benefited from several discussions on x-ray spectroscopy with Dr. R. Burek. The filter calibrations were made possible by the help of Dr. J. Pluth of the University of Chicago Departments of Geophysics and Chemistry. We are grateful for the assistance of E. Drag, Dr. G. Fulks, Dr. G. Hartmann, W. Johnson, R. Petre, and especially S. Jordan. Doctor B. McDaniel, Dr. N. Mistry, Dr. G. Rouse, and the personnel of the Cornell Synchrotron gave us much generous help and support, as did Dr. H. Haggerty and the staff of the Fermi National Accelerator Laboratory. This research was supported in part by NASA Grants NGL 14-001-005 and NGL 14-001-258.

APPENDIX A: EFFECT OF MULTIPLE SCATTERING

Multiple scattering of the incident particles may affect the measured transition radiation intensity in two ways. First, in a narrow solid-angle experiment, it may affect the *detection* of the radiation by broadening the angular distribution of the

incident particles and therefore removing x-rays from the acceptance cone of the detector. This effect has been taken into account in the analysis of the measured frequency spectra in Sec. III. Second, multiple scattering may affect the *emission* of the radiation by modifying the radiation amplitudes at individual interfaces and the phase relations between them. In this section, we derive the conditions under which scattering influences the emission process, and show that these scattering effects are unimportant in our measurements. Garibian[33] and Pafomov[34] have studied the effect at a single vacuum-medium interface, and Ter-Mikaelian[7] has considered the case of a many-foil radiator with dimensions $l_{1,2}$ small compared to the formation zones $Z_{1,2}$ [Eq. (6)]. These results are summarized by Harutyunian and Frangyan,[35] who emphasize the qualitative differences between the single interface and many-foil predictions. A more general discussion without the restriction to small radiator dimensions is required for the experimental results of Sec. III, and is presented below. We consider only the case of electrons.

Scattering must be considered if the average multiple-scattering angle is larger than the angle of emission of radiation:

$$\langle\theta_{MS}^2\rangle \gtrsim \langle\theta_{TR}^2\rangle . \tag{A1}$$

The distance along the particle trajectory over which the radiation is generated is given by the formation zone in the gap material in the forward direction, $Z_2(\theta=0)$ [Eq. (6)]. If the scattering in the gaps is neglected compared to the scattering in the foils, then the scattering develops over a length $l=N_S l_1$ in the foils, where N_S is the number of foils[36] in the length $Z_2(\theta=0)$:

$$N_S=\frac{Z_2(\theta=0)}{l_1+l_2}=\frac{4c}{\omega(l_1+l_2)}\left(\frac{1}{\gamma^2}+\frac{\omega_2^2}{\omega^2}\right)^{-1} .$$

The multiple-scattering angle is given by

$$\langle\theta_{MS}^2\rangle=\frac{\gamma_{MS}^2}{\gamma^2}\frac{l}{L} , \tag{A2}$$

where $\gamma_{MS}^2=4\pi/\alpha=1720$, and L is the radiation length in the foils ($L=49$ cm in polypropylene). Scattering begins to affect the radiation process near the most probable emission angle θ_0 [Eq. (4)]. However, it is reasonable to assume the scattering influence does not become significant until one approaches that angle near which the largest fraction of the radiation is emitted. Numerical computations based on Eq. (9) indicate that this occurs well above θ_0, near

$$\langle\theta_{TR}^2\rangle^{1/2}\approx\chi\theta_{max} , \tag{A3}$$

where $\chi\lesssim 1$, and θ_{max} is defined in Eq. (5). An expression for the average value of θ^2 may be derived from the single-interface distribution (7). In the particular and relevant case $\gamma\omega_2 \ll \omega \ll \gamma\omega_1$, the result is of the form (A3), with χ weakly dependent on ω and γ:

$$\chi=\frac{1}{2[\ln(\gamma\omega_1/\omega)-1]} .$$

For the energies and frequencies in our experiments, χ varies between about 0.3 and 1. With expressions (A2) and (A3) for $\langle\theta_{MS}^2\rangle$ and $\langle\theta_{TR}^2\rangle$, inequality (A1) is satisfied only for frequencies

$$\omega>\omega_{MS}=\frac{\chi^2 L}{4c\gamma_{MS}^2}\left(1+\frac{l_2}{l_1}\right)(\omega_1+\omega_2)^2 . \tag{A4}$$

For the case of polypropylene foils with $l_1=82$ μm and $l_2=1.4$ mm, and for a typical value of $\chi=0.6$, $\omega_{MS}\approx 1.1$ MeV. Scattering is therefore significant only at very high frequencies. Even for smaller values of χ, scattering appears only at frequencies much higher than those in our experiments.

Inequality (A4) is only a necessary condition for scattering to be important. At frequencies above ω_{MS}, the scattering condition (A1) is met only for certain values of γ. For the case of a vacuum-medium interface ($\omega_2=0$), scattering effects are important at Lorentz factors

$$\gamma>\frac{\omega}{\omega_1}\left(\frac{\omega}{\omega_{MS}}-1\right)^{-1} . \tag{A5}$$

In the case $\omega_2>0$, for frequencies near ω_{MS}, (A1) is satisfied for a narrow range of Lorentz factors near

$$\gamma_0=\omega_{MS}/(\omega_1\omega_2)^{1/2} \qquad (\omega\gtrsim\omega_{MS}) , \tag{A6}$$

and for very high frequencies $\omega\gg\omega_{MS}$, scattering is important in the range

$$\gamma_1<\gamma<\gamma_2 \qquad (\omega\gg\omega_{MS}) , \tag{A7}$$

where

$$\gamma_1=(\omega\omega_{MS})^{1/2}/\omega_1 \quad\text{and}\quad \gamma_2=\omega^{3/2}/\omega_2\omega_{MS}^{1/2} .$$

For the numerical example above, $\gamma_0\approx 5\times10^5$, $\gamma_1\approx 5\times10^4(\omega/1.1\text{ MeV})^{1/2}$, and $\gamma_2\approx 4\times10^6(\omega/1.1\text{ MeV})^{3/2}$.

In our experiments in Secs. III and IV (and in most other practical applications using many-foil radiators of plastic or lithium foils, or plastic foam), conditions (A4)–(A7) are not satisfied, and scattering effects on the emission of the radiation can be neglected.

APPENDIX B: DIFFRACTION CRYSTAL EFFICIENCIES

The spectral measurements of Sec. III A were performed with two crystals which were highly reflective over the frequency range 4–30 keV:

pentaerythritol (PET, $2d = 8.726$ Å) and lithium fluoride (LiF, $2d = 2.848$ Å). PET was used from 4 to 11 keV; LiF was used over the entire frequency range. Since the effective width of a crystal (and therefore our reflected counting rate) is largest at small Bragg angles, measurements were generally limited to angles below 30°. A minimum Bragg angle of 8° was used to ensure that the projected cross section of the crystal completely filled the collimator aperture. The surface of the PET crystal was nearly perfect, corresponding to the case of maximum resolution and minimum reflectivity described by the Darwin-Prins dynamical theory of x-ray diffraction.[37] The LiF crystal, on the other hand, was abraded with coarse sandpaper and then blown clean with air in order to approximate a mosaic (ideally imperfect) surface, corresponding to the limiting case of minimum resolution and maximum reflectivity treated by the kinematical theory of x-ray diffraction.[37] Calibration measurements of the actual crystal efficiencies were performed using two techniques: At high frequencies, we used the balanced filter method of Ross[38] to obtain x-rays over a narrow frequency range from a broadband x-ray beam; and at low frequencies, fluorescence lines were used.

The balanced-filter technique is a difference method. By an appropriate choice of thicknesses, the difference in transmitted intensities through two filters (generally of atomic numbers Z and $Z+1$) can be made to vanish at all frequencies except those between the K absorption edges of the two filters. From a beam of white radiation, it is therefore possible to extract just that component falling within the chosen frequency band, with a resolution determined by the separation between neighboring K edges—typically 0.5 to 1 keV. The filters used for these calibrations, together with their K edges, are listed in Table II. The balanced filter method was used over the range 7–30 keV. The crystal efficiency was determined in terms of the effective width $\delta\epsilon$, defined in Sec. III. We measured $\delta\epsilon$ directly by using two filters with K edges separated by the energy interval $\Delta\epsilon_K$. If N_c was the count rate measured with the crystal, averaged over the range between the K edges, and N_d was the count rate measured with the proportional counter directly in the beam (that is, without the crystal), then the effective width was given by $\delta\epsilon = \Delta\epsilon_K N_c/N_d$. Bremsstrahlung beams produced from copper or molybdenum targets were used. The filters were mounted on rotating holders in order to accurately balance their thicknesses along the beam. The uncertainty in the final calibration introduced by the filter balancing was 0.2–4%.

At x-ray energies up to 8 keV, fluorescence line excitation was used to provide a monochromatic beam. In this case, the standard integrated reflectivity R_c was measured, giving the effective width through the relation $\delta\epsilon = \hbar\omega R_c \cot\theta$, where θ is the Bragg angle. These measurements were performed by R. L. Blake and D. M. Barrus at the Los Alamos Scientific Laboratory. The apparatus and similar measurements are described by Burek *et al.*[39] Measurements have been performed down to 4.9 keV for LiF and to 1.5 keV for PET.

Our results are plotted in Fig. 5 and tabulated in Table II. The fluorescence line or filter pair used at each frequency is listed in the table. In Fig. 5, the solid points are determined from the

TABLE II. Crystal-calibration results.

Crystal	Frequency (keV)	Angle		Effective width (eV)	R_c	Fluorescence line	Filter 1	Edge 1 (keV)	Filter 2	Edge 2 (keV)
PET	1.49	72.8°		0.211 (±1.5%)	4.60×10^{-4}	Al $K\alpha$				
	2.62	32.8		0.41 (±2%)	9.97×10^{-5}	Cl $K\alpha$				
	3.69	22.6	(1st order)	1.03 (±2%)	1.16×10^{-4}	Ca $K\alpha$				
	3.69	50.3	(2nd order)	0.026 (±3%)	8.34×10^{-6}	Ca $K\alpha$				
	7.41	11.1		4.3 (±12%)	1.2×10^{-4}		Fe	7.11	Co	7.71
	8.04	10.2	(1st order)	7.2 (±2%)	1.61×10^{-4}	Cu $K\alpha$				
	8.04	20.7	(2nd order)	0.50 (±3%)	2.34×10^{-5}	Cu $K\alpha$				
LiF	4.86	63.5		0.67 (±2%)	2.75×10^{-4}	V $K\alpha$				
	7.41	36.0		1.9 (±12%)	1.8×10^{-4}		Fe	7.11	Co	7.71
	8.04	32.8		2.42 (±2%)	1.94×10^{-4}	Cu $K\alpha$				
	17.55	14.4		17.9 (±14%)	2.6×10^{-4}		Y	17.05	Zr	18.00
	18.49	13.6		17.3 (±12%)	2.3×10^{-4}		Zr	18.00	Nb	18.99
	23.78	10.6		29.9 (±12%)	2.3×10^{-4}		Rh	23.21	Pd	24.36
	26.12	9.60		33.2 (±12%)	2.2×10^{-4}		Ag	25.54	Cd	26.71
	28.56	8.77		38.1 (±12%)	2.1×10^{-4}		In	27.93	Sn	29.18

filter measurements. The major contribution to the uncertainty, up to 10%, came from instability of the beam; filter balancing, counting statistics, and background subtraction added a further 2–4% uncertainty. The open triangles are the results of the fluorescence line calibrations. The rather small uncertainties (±2%) associated with these points are due to the presence of impurity elements in the fluorescence target, electronic noise, and the cosmic-ray background. Theoretical effective widths are also shown for the limiting cases of maximum and minimum reflectivity[40] (mosaic and perfect crystals, respectively). As expected, the measured points fall inside the theoretical envelope. The PET points lie fairly close to the perfect crystal curve at low frequencies, while the LiF results fall near the mosaic limit. The deviations of the real crystals from the ideal curves depend on the detailed crystal defect structures.[40] A fit to the measured data points was used as the actual efficiency. In the range 9–17 keV, where there are no appropriate filter pairs, we have used an extrapolation of our measurements at lower and higher frequencies; we estimate an uncertainty in the effective width of, at most, 20% in that range.

---

*Submitted to the Department of Physics, University of Chicago, Chicago, Illinois, in partial fulfillment of the requirements for the Ph.D. degree.

†Present address: Department of Physics, University of New Hampshire, Durham, New Hampshire 03824.

[1]G. Hartmann, D. Müller, and T. Prince, Phys. Rev. Lett. 38, 1368 (1977); and T. Prince, Ph. D. thesis, University of Chicago, 1977 (unpublished).

[2]J. Cobb, C. W. Fabjan, S. Iwata, C. Kourkoumelis, A. J. Lankford, G.-C. Moneti, A. Nappi, R. Palmer, P. Rehak, W. Struczinski, and W. Willis, Nucl. Instrum. Methods 140, 413 (1977).

[3]R. W. Ellsworth, A. S. Ito, J. R. MacFall, F. Siohan, R. E. Streitmatter, S. C. Tonwar, and G. B. Yodh, in *Proceedings of the Fourteenth International Conference on Cosmic Rays, Munich, 1975,* edited by Klaus Pinkau (Max-Planck-Institute, Münich, 1975), Vol. 7, p. 2538.

[4]M. L. Cherry, G. Hartmann, D. Müller, and T. A. Prince, Phys. Rev. D 10, 3594 (1974).

[5]G. M. Garibian, Zh. Eksp. Teor. Fiz. 39, 1630 (1960) [Sov. Phys.—JETP 12, 1138 (1961)].

[6]J. D. Jackson, *Classical Electrodynamics* (Wiley, New York, 1975).

[7]M. L. Ter-Mikaelian, *High-Energy Electromagnetic Processes in Condensed Media* (Wiley, New York, 1972).

[8]G. M. Garibian, Zh. Eksp. Teor. Fiz. 33, 1403 (1957) [Sov. Phys.—JETP 6, 1079 (1958)].

[9]G. M. Garibian, Zh. Eksp. Teor. Fiz. 37, 527 (1959) [Sov. Phys.—JETP 37, 372 (1960)].

[10]G. M. Garibian, Yerevan Physical Institute Scientific Report No. EFI 27 (73), 1973 (unpublished); and in *Proceedings of the International Conference on Instrumentation for High Energy Physics, Frascati, 1973,* edited by Stanislao Stipcich (Laboratori Nazionali del Comitato Nazionale per l'Energia Nucleare, Frascati, 1973).

[11]M. L. Ter-Mikaelian, Nucl. Phys. 24, 43 (1961).

[12]G. M. Garibian, Zh. Eksp. Teor. Fiz. 60, 39 (1971) [Sov. Phys.—JETP 33, 23 (1971)].

[13]X. Artru, G. Yodh, and G. Mennessier, Phys. Rev. D 12, 1289 (1975).

[14]R. Ellsworth, J. MacFall, G. Yodh, F. Harris, T. Katsura, S. Parker, B. Peterson, L. Shiraishi, V. Stenger, J. Mulvey, B. Brooks, and J. Cobb, in *Proceedings of the Thirteenth International Conference on Cosmic Rays, Denver, 1973* (Colorado Associated Univ. Press, Boulder, 1973), Vol. 4, p. 2819.

[15]J. Fischer, S. Iwata, V. Radeka, C. L. Wang, and W. Willis, Phys. Lett. 49B, 393 (1974).

[16]C. Camps, V. Commichau, M. Deutschmann, H. Göddeke, K. Hangarter, W. Liesmann, U. Pützhofen, and R. Schulte, Nucl. Instrum. Methods 131, 411 (1975).

[17]L. C. L. Yuan, C. L. Wang, H. Uto, and S. Prünster, Phys. Lett. 31B, 603 (1970).

[18]A. A. Frangian, F. R. Harutjunian, V. P. Kishinevski, A. A. Nazarian, and G. B. Torgomian, in Proceedings of the International Conference on Instrumentation for High Energy Physics, Dubna, 1970 (unpublished); see also Ref. 7, Sec. 29f.

[19]K. Hoshino, Y. Ohashi, A. Okada, K. Taira, and K. Yokoi, in *Proceedings of the Eleventh International Conference on Cosmic Rays, Budapest, 1969,* edited by P. Gombás [Acta. Phys. Acad. Sci. Hung. 29, Suppl. 4, 443 (1970)].

[20]C. W. Fabjan and W. Struczinski, Phys. Lett. 57B, 483 (1975).

[21]C. W. Fabjan, Nucl. Instrum. Methods 146, 343 (1977).

[22]A. I. Alikhanian, S. A. Kankanian, A. G. Oganessian, and A. G. Tamanian, Phys. Rev. Lett. 30, 109 (1973).

[23]R. Bosshard, J. Fischer, S. Iwata, V. Radeka, C. L. Wang, and M. Atac, Nucl. Instrum. Methods 127, 141 (1975).

[24]L. C. L. Yuan, P. W. Alley, G. F. Dell, R. Keller, and H. Uto, Nucl. Instrum. Methods 130, 45 (1975).

[25]T. A. Prince, D. Müller, G. Hartmann, and M. L. Cherry, Nucl. Instrum. Methods 123, 231 (1975).

[26]Artru *et al.* (Ref. 13) present expressions (14a) and (14c) on the basis of numerical computations. Cherry *et al.* (Ref. 4) give a different expression for γ_S which does not depend on ω or l_1. Their expression overestimates γ_S for large values of $l_2/l_1 > 60$ and underestimates γ_S for $l_2/l_1 < 60$.

[27]B. Henke, R. L. Elgin, R. E. Lent, and R. B. Ledingham, Norelco Reporter 14, 112 (1967).

[28]E. Storm and H. I. Israel, Los Alamos Scientific Laboratory Report No. LA-3753, 1967 (unpublished).

[29]M. L. Cherry and D. Müller, Phys. Rev. Lett. 38, 5 (1977).

[30]G. M. Garibian, L. A. Gevorgyan, and C. Yang, Zh. Eksp. Teor. Fiz. 66, 552 (1974) [Sov. Phys.-JETP 39,

265 (1974)].
[31]D. Müller and M. L. Cherry, in Proceedings of the International Symposium on Transition Radiation of High Energy Particles, Yerevan, 1977 (unpublished).
[32]M. L. Cherry, G. Hartmann, D. Müller, and T. Prince, in Proceedings of the Fifteenth International Conference on Cosmic Rays, Plovdiv, 1977 (unpublished).
[33]G. M. Garibian, Zh. Eksp. Teor. Fiz. 39, 332 (1960) [Sov. Phys.—JETP 12, 237 (1961)].
[34]V. E. Pafomov, Zh. Eksp. Teor. Fiz. 47, 530 (1964) [Sov. Phys.—JETP 20, 353 (1965)].
[35]F. R. Harutyunian and A. A. Frangyan, Academy of Sciences Armenian SSR Report No. IPhR-75-22, 1975 (unpublished).
[36]To within a factor π, this is the same expression given by Cherry *et al.* (Ref. 4) for the minimum number of foils for which Eq. (9) could be integrated analytically over angles to yield the resulting many-foil spectrum (11). See also Garibian (Ref. 10); and V. I. Zatsepin, in *Proceedings of the Thirteenth International Conference on Cosmic Rays, Denver, 1973* (Colorado Associated Univ. Press, Boulder, 1973), Vol. 4, p. 2842.
[37]W. H. Zachariasen, *Theory of X-Ray Diffraction in Crystals* (Wiley, New York, 1945).
[38]P. A. Ross, J. Opt. Soc. Am. 16, 433 (1928).
[39]A. J. Burek, D. M. Barrus, and R. L. Blake, Astrophys. J. 191, 533 (1974).
[40]A. J. Burek, Ph.D. thesis, University of Chicago, 1975 (unpublished); and private communication.